做科研，非一朝一夕

买器材，应速战速决

Newport数千种优质产品当日发货，
更多惊喜尽在PhotonSpeed™光速购！

mks | Newport™

High-order harmonic generation from zigzag graphene nanoribbons

Jiaqi Wu (吴家其)[1,2], Yinghui Zheng (郑颖辉)[2,*], Zhinan Zeng (曾志男)[2,], and Ruxin Li (李儒新)[1,2]**

[1]*School of Physical Science and Technology, ShanghaiTech University, Shanghai 201210, China*
[2]*State Key Laboratory of High Field Laser Physics, Shanghai Institute of Optics and Fine Mechanics, Chinese Academy of Sciences, Shanghai 201800, China*
**Corresponding author: yhzheng@siom.ac.cn; **corresponding author: zhinan_zeng@mail.siom.ac.cn*
Received May 6, 2020; accepted June 23, 2020; posted online August 28, 2020

High-order harmonic generation originated from zigzag graphene nanoribbons (ZGNRs) induced by intense laser pulses is investigated theoretically. During the interaction between the intense mid-infrared laser and the ZGNR, we find that localized edge states mainly contribute to the generation of the low-order harmonics, while cutoff harmonics result from the other confined states. Our result shows that the edge-state effect of ZGNR with narrow width can enhance the conversion efficiency of low-order harmonics, rather than the higher-order harmonics extended to the cutoff region.

Keywords: graphene nanoribbons; high-order harmonic generation; edge state.
doi: 10.3788/COL202018.103201.

The extreme nonlinear phenomenon of high-order harmonic generation (HHG) has been studied extensively since its first experimental discovery[1–3]. According to the semiclassical three-step model of atomic HHG, an electron first tunnel ionizes out of the Coulomb potential barrier. Then, it gains extra kinetic energy when accelerating in the external field. Finally it emits a high-energy harmonic photon when recombining with its parent ion[4]. The supercontinuum region of the HHG plateau can be used in the generation of isolated attosecond pulses, which is intended for probing ultrafast atomic and molecular motion[5–7]. However, advances in attosecond science to date mostly focus on HHG with rare gases[8–12].

Since the first, to the best of our knowledge, experiment of solid-state HHG[13,14], both experimental[15–18] and theoretical work[19–21] of different solid-state systems have been done to study the essence of HHG from solids. It is widely accepted that HHG in solids originates from two channels, namely interband and intraband currents. Like the atomic HHG three-step model, the mechanism of interband current can be explained by a recombining model: an electron–hole pair is created from the interband transition, and then electrons and holes are accelerated by the laser field. When an electron and a hole recombine together, a high-order harmonic photon will be emitted. The other solid-state HHG mechanism is intraband current, which originates from Bloch oscillations within the same band[22].

Recently, there has been a growing interest in studying HHG from different crystal nanostructures. McDonald *et al.* demonstrated that the HHG efficiency increases due to the quantum confinement in a model quantum nanowire[23]. Cox *et al.* studied plasmon-assisted HHG originating from doped graphene nanostructures and indicated that localized plasmons give rise to the HHG conversion efficiencies[24]. Due to the nanoscale confinement effects, HHG has been reported to be efficiently enhanced in these nanostructures.

Besides, studying the electronic properties of nanoscale graphene systems has attracted much attention in favor of developing next-generation electronic devices. HHG in two-dimensional (2D) material graphene has been intensively studied both theoretically[25–32] and experimentally[33–36]. However, localized quantum effects on the HHG generated from nanoscale graphene systems interacting with a high-intensity laser field have not been investigated yet. The broken translational symmetry at edges and boundaries of 2D atomic materials like graphene and transition metal dichalcogenides leads to exceptional physical phenomena and applications in nonlinear optics[37–40]. Armchair and zigzag edges are the two kinds of graphene edges, which have a 30° difference in their orientation in a single-layer graphene sheet. Specifically, the zigzag graphene edge exhibits distinguished localized electronic states, which the armchair edge does not possess[41,42]. Due to the confinement of finite-sized nanostructure of zigzag graphene nanoribbons (ZGNRs), the electron wave function may be affected by the quantum localization of edges and introduce many brand-new strong field physical phenomena.

In this work, HHG spectra originating from the interaction of ZGNR with intense laser pulses have been theoretically studied by numerically solving the time-dependent Schrödinger equation (TDSE). In this work, because the pulse duration is about 100 fs for the 3.6 μm laser pulse, which is much shorter than the electron–electron (e-e) scattering time[31,36], we can ignore this process in the simulation. Furthermore, for simulations including the e-e scattering process, one needs to adopt the density matrix model such as solving the semiconductor Bloch equation (SBE)[22]. The total number of conduction bands

is N, which is the number of zigzag carbon lines in ZGNR. As shown in Ref. [15], Wu *et al.* also used TDSE in the velocity gauge to simulate the HHG process in a model band. They considered that the TDSE model is valid enough for laser wavelengths between 2 and 5 μm. Similarly, we alter the wavelength of the incident laser from 800 nm to 3.6 μm, and the peak intensity is chosen to be 1 TW/cm^2. The HHG spectra are highly dependent on the width N of ZGNR. We also investigate the distinct edge-state effect on the low-order harmonics yield of ZGNR induced by mid-infrared (MIR) pulses.

To investigate the high-order harmonics generated by ZGNR, we use the TDSE in the velocity gauge to simulate the interaction between the intense laser pulses and ZGNR[43,44]. In this model, the Schrödinger equation can be written as

$$i\hbar\frac{\partial}{\partial t}|\psi_k(x,t)\rangle=\left[H_0+\frac{e}{m_0}A(t)p_x\right]|\psi_k(x,t)\rangle, \quad (1)$$

where e and m_0 are the charge and mass of the free electron. $A(t)=E_0/\omega_0\sin^2(\pi t/T)\cos(\omega_0 t)$ is the vector potential of incident laser pulses, where T is the total time of the simulation. For all simulations in this work, T is 16 optical cycles. $p_x=-i\hbar\partial/\partial_x$ is the momentum operator. For each value of the quasi-momentum k, the electron wave function is represented on the basis of Bloch states $|\varphi_k^n(x)\rangle$, n is a band index, and k is the electron wave vector, which can be evaluated by solving the single-electron stationary Schrödinger equation with an unperturbed Hamiltonian H_0. Then, the total electron wavefunction in Eq. (1) can be written as

$$|\psi_k(x,t)\rangle=\sum_{n=1}^{N_{\max}}\alpha_k^n(t)|\varphi_k^n(x)\rangle, \quad (2)$$

where $N_{\max}$ is the plane wave number. Substituting ansatz Eq. (2) into Eq. (1), the time-dependent coefficients $\alpha_k^n(t)$ are evaluated by solving the following coupled differential equation:

$$i\hbar\frac{\partial\alpha_k^q(t)}{\partial t}=E_k^q\alpha_k^q(t)+\frac{e}{m_0}A(t)\sum_{l=1}^{N_{\max}}p_k^{ql}\alpha_k^l(t), \quad (3)$$

where $p_k^{ql}=\langle\varphi_k^q|p_x|\varphi_k^l\rangle$ is the momentum matrix. To obtain the HHG, we need to calculate the electron current induced by the laser field in the ZGNR. The single-electron contributions to the current density over a unit cell can be presented as follows:

$$j_k(t)=-\frac{e}{m_0}\frac{1}{\Omega}\int_\Omega \mathrm{d}x\{\mathrm{Re}[\psi_k^*(x,t)p_x\psi_k(x,t)] + eA(t)|\psi_k(x,t)|^2\}, \quad (4)$$

where Ω is the volume of a unit cell of ZGNR. With the substitution of Eq. (2), the single-electron current density can be presented as follows:

$$j_k(t)=-\frac{e}{m_0}\left\{\mathrm{Re}\left\{\sum_{q,l}[\alpha_k^q(t)]^*\alpha_k^l(t)p_k^{ql}\right\}+eA(t)\right\}, \quad (5)$$

and the total current density can be integrated as $j(t)=\int j_k(t)\mathrm{d}k$. Thus, the intensity of the harmonic emission $S(q\omega)$ written as Eq. (6) at the qth harmonic frequency $q\omega$ is dependent on the absolute square of the Fourier transform of the total current density denoted as $J(q\omega)=q\omega\int_{-\infty}^{\infty}j(t)\exp(-iq\omega t)\mathrm{d}t$:

$$S(q\omega)=|J(q\omega)|^2. \quad (6)$$

For ZGNR, with tight-binding (TB) approximation, the single-electron stationary Schrödinger equation can be written as

$$H_0|\varphi_k^n(x)\rangle=E_k^n|\varphi_k^n(x)\rangle. \quad (7)$$

Although the simple TB model cannot describe the real ZGNR accurately, in our work, we focus on discussing the feature of the harmonic spectra, the contribution of different electron states, etc. We choose this TB model because it has been carefully investigated, discussed, and proved to be valid[41,45,46]. It is simple enough to help us in discussing and understanding the contribution of different electronic states in ZGNR, so we use it to calculate the band structure of ZGNR and analyze the contribution of the different Bloch states to the generation of high harmonics. The band structure of ZGNR composed of N zigzag carbon lines can be calculated by numerically diagonalizing the following tridiagonal $2N\times 2N$ Hamiltonian matrix with alternating off-diagonal elements[45,47]:

$$H_0=\begin{pmatrix} 0 & 2\cos\left(\frac{ka}{2}\right) & 0 & 0 & 0 & \cdots \\ 2\cos\left(\frac{ka}{2}\right) & 0 & 1 & 0 & 0 & \cdots \\ 0 & 1 & 0 & 2\cos\left(\frac{ka}{2}\right) & 0 & \cdots \\ 0 & 0 & 2\cos\left(\frac{ka}{2}\right) & 0 & 1 & \cdots \\ 0 & 0 & 0 & 1 & 0 & \cdots \\ \vdots & \vdots & \vdots & \vdots & \vdots & \vdots \end{pmatrix}. \quad (8)$$

After diagonalizing the unperturbed Hamiltonian matrix H_0, we can get ZGNR's band structure and the momentum matrix further. As Fig. 1(a) depicts, N defines the number of zigzag carbon lines in ZGNR, and $a=2.46$ a.u. is the lattice constant of graphene. Figs. 1(b) and 1(c) show the band structure of ZGNR with $N=4$ and $N=15$, respectively. As stated in Ref. [41], the energy bands present some typical features, e.g., the Dirac points of the 2D graphene are mapped into $k=\pm 2\pi/(3a)$, and there are two partially flat degenerate bands with zero energy between the Dirac points and the border of the Brillouin zone (BZ). The corresponding electronic states are mainly located at the edges, and the bands are highly degenerate at the borders of the BZ.

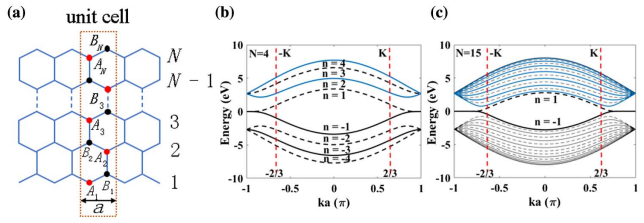

Fig. 1. (a) Crystal structure and unit cell of ZGNR composed of N zigzag carbon lines. (b), (c) Band structure of ZGNR whose width is 4 and 15 used in our simulations.

We mark the bands with different numbers in Figs. 1(b) and 1(c). For the bands above the Fermi level (0 eV in the figures), they are $n = 1, 2, \ldots$. For the bands below the Fermi level, they are the opposite. As shown in a previous work[46], the ZGNR has some very special features such as the edge states. In Figs. 1(b) and 1(c), the Bloch states between the border of the BZ ($|ka| = \pi$) and the |K| points ($|ka| = 2\pi/3$) on bands $n = \pm 1$ indicate the edge states, while all the others represent the confined states. These edge states mean strongly localized states in the flat bands. We tend to see its effect on the generation of high-order harmonics. In all our numerical simulations, 601 points are used for the k vector (total BZ). Initially, the electron is set on the $n = -1$ band (the upmost valence band). Only the bands with positive n and $n = -1$ are considered. As shown in Ref. [47], the transition between the adjacent dashed–solid bands is forbidden, which means the transition between the solid line bands and the dashed line bands is forbidden. As depicted in Figs. 1(b) and 1(c), for $N = 4$, although all the bands of $n > 0$ are considered as conduction bands, electrons can only be excited to $n = 2, 4$ bands [blue solid lines in Fig. 1(b)]. For $N = 15$, electrons can only be excited up to $n = 2, 4, 6, 8, 10, 12, 14$ bands [blue solid lines in Fig. 1(c)] because of the forbidden transition.

First, Figs. 2(a) and 2(b) show the typical harmonic spectra generated by lasers with different wavelengths under the intensity of 1 TW/cm^2. For the case of 800 nm, the harmonic spectrum represents the exponential decrease as the traditional perturbative harmonics. As depicted in Fig. 2(c), the cutoff energy of the harmonic spectra shows a linear dependence on the wavelength, which is in good agreement with a previous research work[48]. The clear plateau can be seen in Fig. 2(b), which indicates the strong field effect.

The main purpose of this work is to investigate the contribution of the edge states to ZGNR's HHG. To achieve this, we can initially set the electron population between $k = \pm 2\pi/3$ to be zero in the simulation. In such a case, only localized edge states in the upmost valence band are considered in the calculation, while all the other states in the valence bands are excluded. Then, we can compare its generated harmonic spectra with the normal harmonic spectra, where electrons in the upmost valence band between $k = \pm\pi$ are populated initially. In this part, we set the laser intensity to be 1 TW/cm^2 and the laser wavelength to be 3600 nm. In the simulations, all of the states in the conduction bands are involved in the process of HHG. With the increase of the width N, the number of the conduction bands will be larger. Figure 3 shows the harmonic spectra of ZGNRs with different widths, where the blue solid curve denotes the normal harmonic spectrum, and the red dashed curve denotes the contribution of the edge states in each figure.

For the low harmonics (below ninth harmonic), the red dashed curves are mostly higher than the blue solid curves. It is the result of interference with the electrons initially localized in the region of $k < |\mathrm{K}|$, which decreases the generation of the low-order harmonics in the normal harmonic spectra. It is notable that the red dashed curves still show a well-defined plateau region when $N < 4$. In these cases, although the ratio of edge states is less than that of larger N, electrons initially localized in the region of $k > |\mathrm{K}|$ contribute to the HHG process mainly. Until the N is large enough, e.g., larger than 15, they become almost the same. As we know from the previous work[41], the flatness index of the zero-energy bands in ZGNR increases with the number N at first, reaches the highest value at $N = 7$, and then decreases. This means the low-order harmonics are mainly generated by the edge states. Because when $N = 2$ or $N = 3$, the bands are not flat enough, so the electrons will not be localized in the region of $k > |\mathrm{K}|$, and thus the edge-state effect is small.

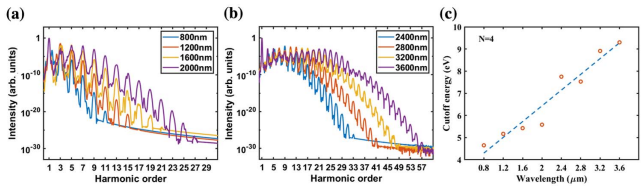

Fig. 2. (a), (b) Intensity variation of HHG with the pump laser wavelength ranging from 800 nm to 3600 nm. The ZGNR width N is four and the pump laser intensity is 1 TW/cm^2. (c) Wavelength linear dependence of the cutoff energy in ZGNR's HHG.

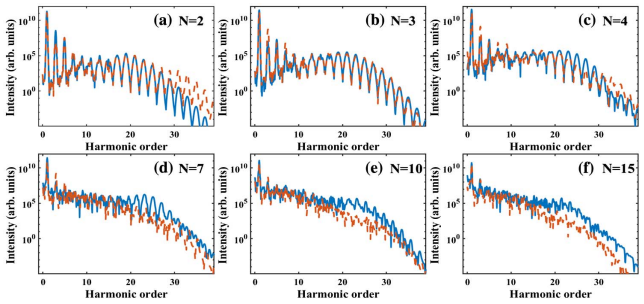

Fig. 3. (a)–(f) High harmonic spectra of ZGNR with different widths ($N = 2$, 3, 4, 7, 10, 15), where the blue solid curves denote the normal harmonic spectra, and the red dashed curves represent the harmonic spectra contributed only by the edge states.

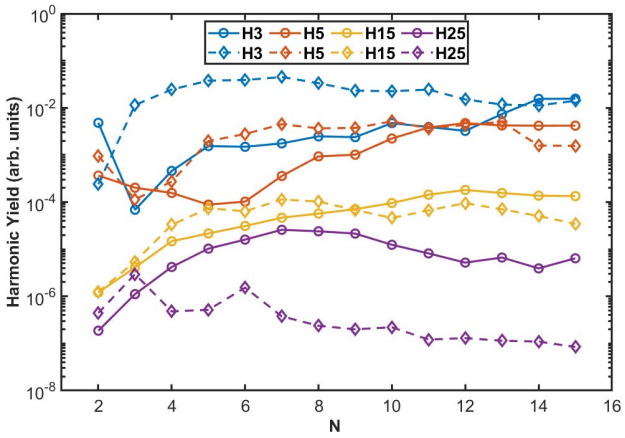

Fig. 4. Typical yield of 3rd, 5th, 15th, and 25th harmonics, depending on the ZGNR width. The solid lines marked with circles are the normal harmonics, while the dashed curves with diamond marks denote harmonics yield generated only by edge states.

For the harmonics in the cutoff region (around the 25th harmonic), the situation is different. When N is small, the cutoff harmonics are weak for both curves. With the increase of ZGNR width (N number), the blue solid curves become increasing, but the red dashed curves decrease further. This means, for narrow ZGNR, the efficiency of the cutoff harmonics is small. With the increase of the N number, the cutoff harmonics can be produced efficiently, but it is mainly from the confined states, rather than the edge states. To make it clear, we choose several harmonics to compare their yield, as shown in Fig. 4.

Figure 4 shows the yield of the 3rd, 5th, 15th, and 25th harmonics, depending on the ZGNR width. They are generated by the 3600 nm MIR laser, as shown in Fig. 3. We integrate the harmonic spectra between adjacent harmonics of each harmonic, e.g., integrating the harmonic spectra between the second and fourth harmonics to represent the yield of the third harmonic. The solid curves marked with circles are the normal harmonics, while the dashed curves marked with diamonds are the harmonics generated only by edge states. For all harmonics at small N, the solid curves and the corresponding dashed curves almost have the same value. But for low-order harmonics, e.g., third and fifth, the dashed curves will be higher than the solid curves between $N = 4$ and $N = 10$. Combining with the discovery of Ref. [41] where the effect of edge states is maximal only when $N = 7$, we also find that the yield of the harmonics generated from the edge states seems to be similar with that from other confined states for ZGNR widths $N = 2, 3, 4$. For these ZGNR widths, the ratio of edge states is smaller than in the case $N = 7$ according to Ref. [41]; thus, the effect of edge states is not obvious. In addition, around $N = 7$, for the low-order harmonics (the third and fifth harmonics), the difference between the normal harmonic yield and harmonic yield generated by edge states is relatively large, so it means that the contribution of edge states is the main one. With the increase of harmonic order, up to the 15th harmonic, the two curves are close, so that is to say the contribution of edge states is almost equivalent to that of confirmed states. For the higher harmonic orders, the contribution of the edge state can be completely ignored. Thus, edge states of ZGNR mainly contribute to the generation of low-order harmonics. When the number N becomes larger, their yield will become comparable again. For the 15th harmonic in the middle region of the spectra, the dashed curve is larger than the solid curve, while it becomes the opposite when $N > 9$. But for the 25th harmonic in the cutoff region, the solid curve is almost always larger than the dashed curve for more than one order of magnitude.

In conclusion, we have investigated HHG in ZGNR driven by a strong laser field from near-infrared to MIR wavelengths based on one-dimensional TDSE. The simulated HHG spectra show a high relevance with the width of ZGNR. We demonstrate that low-order harmonics are mainly generated by the edge states of ZGNR, but the cutoff harmonics are mainly produced by the confined states for the MIR laser at the 3600 nm wavelength and 1 TW/cm^2 intensity. Due to the relative high density of electronic states near the Fermi energy, edge states confined in the flat band regions of ZGNR will be an effective way to enhance the low-order harmonics.

This work was supported by the National Natural Science Foundation of China (Nos. 91950203, 11874374, 11574332, 61690223, and 11774363), the Strategic Priority Research Program of the Chinese Academy of Sciences (No. XDB16), and the Chinese Academy Sciences (CAS) Youth Innovation Promotion Association.

References

1. A. McPherson, G. Gibson, H. Jara, U. Johann, T. S. Luk, I. A. McIntyre, K. Boyer, and C. K. Rhodes, J. Opt. Soc. Am. B: Opt. Phys. **4**, 595, (1987).
2. P. B. Corkum and F. Krausz, Nat. Phys. **3**, 381 (2007).
3. F. Krausz and M. Ivanov, Rev. Mod. Phys. **81**, 163 (2009).
4. P. B. Corkum, Phys. Rev. Lett. **71**, 1994 (1993).
5. M. Hentschel, R. Kienberger, Ch Spielmann, G. A. Reider, N. Milosevic, T. Brabec, P. Corkum, U. Heinzmann, M. Drescher, and F. Krausz, Nature **414**, 509 (2001).
6. M. Drescher, M. Hentschel, R. Kienberger, M. Uiberacker, V. Yakovlev, and A. Scrinzi, Nature **419**, 803 (2002).
7. G. Marcus, W. Helml, X. Gu, Y. Deng, R. Hartmann, T. Kobayashi, L. Strueder, R. Kienberger, and F. Krausz, Phys. Rev. Lett. **108**, 023201 (2012).
8. G. Sansone, E. Benedetti, F. Calegari, C. Vozzi, L. Avaldi, R. Flammini, L. Poletto, P. Villoresi, C. Altucci, R. Velotta, S. Stagira, S. D. Silvestri, and M. Nisoli, Science **314**, 443 (2006).
9. X. Feng, S. Gilbertson, H. Mashiko, H. Wang, S. D. Khan, M. Chini, Y. Wu, K. Zhao, and Z. Chang, Phys. Rev. Lett. **103**, 183901 (2009).
10. M. Chini, K. Zhao, and Z. Chang, Nat. Photon. **8**, 178 (2014).
11. L. He, G. Yuan, K. Wang, W. Hua, C. Yu, and C. Jin, Photon. Res. **7**, 1407 (2019).
12. J. Xue, C. Liu, Z. Zeng, R. Li, and Z. Xu, Chin. Opt. Lett. **17**, 082601 (2019).
13. S. Ghimire, A. D. DiChiara, E. Sistrunk, P. Agostini, L. F. DiMauro, and D. A. Reis, Nat. Phys. **7**, 138 (2011).
14. S. Ghimire and D. A. Reis, Nat. Phys. **15**, 10 (2019).

15. M. Wu, S. Ghimire, D. A. Reis, K. J. Schafer, and M. B. Gaarde, Phys. Rev. A **91**, 043839 (2015).
16. P. G. Hawkins and M. Y. Ivanov, Phys. Rev. A **87**, 063842 (2013).
17. N. Moiseyev, Phys. Rev. A **91**, 053811 (2015).
18. T. Higuchi, M. Stockman, and P. Hommelhoff, Phys. Rev. Lett. **113**, 213901 (2014).
19. T. T. Luu and H. J. Wörner, Nat. Commun. **9**, 916 (2018).
20. G. Vampa, T. J. Hammond, N. Thiré, B. E. Schmidt, F. Légaré, C. R. McDonald, T. Brabec, D. D. Klug, and P. B. Corkum, Phys. Rev. Lett. **115**, 193603 (2015).
21. C. Liu, Y. Zheng, Z. Zeng, and R. Li, Phys. Rev. A **93**, 043806 (2016).
22. G. Vampa and T. Brabec, J. Phys. B: At. Mol. Opt. Phys. **50**, 083001 (2017).
23. C. R. McDonald, K. S. Amin, S. Aalmalki, and T. Brabec, Phys. Rev. Lett. **119**, 183902 (2017).
24. J. D. Cox, A. Marini, and F. J. G. de Abajo, Nat. Commun. **8**, 14380 (2017).
25. K. L. Ishikawa, Phys. Rev. B **82**, 201402 (2010).
26. S. I. Simonsen, S. A. Sørngård, M. Førre, and J. P. Hansen, J. Phys. B: At. Mol. Opt. Phys. **47**, 065401 (2014).
27. I. Al-Naib, J. E. Sipe, and M. M. Dignam, Phys. Rev. B **90**, 245423 (2014).
28. R. A. Ganeev, E. Fiordilino, D. Cricchio, P. P. Corso, M. Suzuki, S. Yoneya, and H. Kuroda, Laser Phys. Lett. **12**, 065401 (2015).
29. I. Al-Naib, J. E. Sipe, and M. M. Dignam, New J. Phys. **17**, 113018 (2015).
30. L. A. Chizhova, F. Libisch, and J. Burgdörfer, Phys. Rev. B **95**, 085436 (2017).
31. L. A. Chizhova, F. Libisch, and J. Burgdörfer, Phys. Rev. B **94**, 075412 (2016).
32. C. Liu, Y. Zheng, Z. Zeng, and R. Li, Phys. Rev. A **97**, 063412 (2018).
33. P. Bowlan, E. Martinez-Moreno, K. Reimann, T. Elsaesser, and M. Woerner, Phys. Rev. B **89**, 041408 (2014).
34. N. Yoshikawa, T. Tamaya, and K. Tanaka, Science **356**, 736 (2017).
35. M. Taucer, T. J. Hammond, P. B. Corkum, G. Vampa, C. Couture, N. Thiré, B. E. Schmidt, F. Légaré, H. Selvi, N. Unsuree, B. Hamilton, T. J. Echtermeyer, and M. A. Denecke, Phys. Rev. B **96**, 195420 (2017).
36. M. Baudisch, A. Marini, J. D. Cox, T. Zhu, F. Silva, S. Teichmann, M. Massicotte, F. Koppens, L. S. Levitov, F. J. García de Abajo, and J. Biegert, Nat. Commun. **9**, 1018 (2018).
37. W. Yao, S. A. Yang, and Q. Niu, Phys. Rev. Lett. **102**, 096801 (2009).
38. X. Yin, Z. Ye, D. A. Chenet, Y. Ye, K. O'Brien, J. C. Hone, and X. Zhang, Science **344**, 488 (2014).
39. C. Lian, M. Guan, S. Hu, J. Zhang, and S. Meng, Adv. Theory Simul. **1**, 1870018 (2018).
40. J. Guo, H. Zhong, B. Yan, Y. Chen, Y. Jiang, T. Wang, J. Shao, C. Zheng, and X.-S. Liu, Phys. Rev. A **93**, 033806 (2016).
41. K. Nakada, M. Fujita, G. Dresselhaus, and M. S. Dresselhaus, Phys. Rev. B **54**, 17954 (1996).
42. K. Wakabayashi, K. Sasaki, T. Nakanishi, and T. Enoki, Sci. Technol. Adv. Mater. **11**, 054504 (2010).
43. M. Korbman, S. Y. Kruchinin, and V. S. Yakovlev, New J. Phys. **15**, 013006 (2013).
44. Z. M. Jia and Y. D. Peng, J. Phys. Commun. **2**, 065006 (2018).
45. A. Cresti, N. Nemec, B. Biel, G. Niebler, F. Triozon, G. Cuniberti, and S. Roche, Nano Res. **1**, 361 (2008).
46. C. Salazar, J. L. Cheng, and J. E. Sipe, Phys. Rev. B **93**, 075442 (2016).
47. S. M.-M. Dubois, Z. Zanolli, X. Declerck, and J.-C. Charlier, Eur. Phys. J. B **72**, 1 (2009).
48. X. Liu, X. Zhu, X. Zhang, D. Wang, P. Lan, and P. Lu, Opt. Express **25**, 29216 (2017).